ELSEVIER

Physica D 97 (1996) 133–154

PHYSICA D

Patterns and spatiotemporal chaos in parametrically forced surface waves: a systematic survey at large aspect ratio

A. Kudrolli [a], J.P. Gollub [a,b,*]

[a] *Department of Physics, Haverford College, Haverford, PA 19041, USA*
[b] *Physics Department, University of Pennsylvania, Philadelphia PA 19104, USA*

Abstract

A systematic experimental survey of both the primary patterns and the secondary instabilities of parametrically forced surface waves (Faraday waves) in the large system limit is presented. The symmetry of the primary pattern (stripes, squares, or hexagons) depends on viscosity ν and driving frequency f_0. Hexagons are observed at low f_0 over the whole viscosity range despite the subharmonic symmetry that tends to suppress them. Possible mechanisms for the occurrence of hexagons for single frequency forcing are discussed. Boundary-induced distortion is absent for the hexagonal and square patterns, but present for stripes. *Phase defects* occur between hexagonal domains differing in temporal phase by π (with respect to the forcing). Patterns of different symmetry *coexist* in certain parameter ranges. The transition to *spatiotemporal chaos* (STC) depends on the symmetry of the primary patterns. The hexagonal patterns undergo an order/disorder transition in which the angular anisotropy in Fourier space declines continuously to zero. Striped patterns at high viscosity become unstable via transverse amplitude modulations in regions of high curvature; this instability results in a spatially nonuniform *mixed state* in which domains of STC coexist with stripes. We propose that this phenomenon may be understood in terms of a *critical curvature* that depends on the acceleration. A secondary oscillatory instability is also observed to deform the stripes within the mixed state at intermediate viscosities.

PACS: 47.54.+r; 47.52.+j; 47.35+i
Keywords: Hydrodynamics; Surface waves; Patterns; Spatiotemporal chaos

1. Introduction

Much of the progress achieved over the past two decades in understanding pattern formation in nonlinear systems stems from extensive theoretical and experimental efforts directed at several well-defined hydrodynamic systems: Rayleigh–Bénard convection; convection in binary mixtures; and Taylor–Couette flow. Each of these, viewed mathematically, is a multiparameter bifurcation problem with at least two control parameters. Substantial progress has been realized particularly for situations in which the spatial variations are primarily two-dimensional (large layers) or one-dimensional (annuli). The state of the field as of early 1993 was reviewed by Cross and Hohenberg [1].

The interesting case of parametrically forced surface waves induced by vertical oscillation of the container, first studied by Faraday, has been studied somewhat less systematically in the "large system" limit that is most relevant to the problems of pattern formation, secondary instability and spatiotemporal chaos (STC). This system is potentially attractive for

* Corresponding author.

PII S0167-2789(96)00099-1

several reasons. First, the basic time scale for the evolution of patterns is typically of orders of magnitude *shorter* than the case for thermal convection, so that a multi-dimensional parameter space can be explored in a reasonable time. Second, the wave number of the basic pattern can be controlled experimentally via the imposed forcing frequency. This capability allows direct testing of the wave number dependence of stability properties in a way that is more straightforward than the imposition of controlled initial or boundary conditions, which is generally required for other systems. Varying the driving frequency also allows one to explore subtle effects that occur in the transition between the gravity and capillary wave regimes. Third, all of the basic pattern symmetries can be realized near onset, including stripes or one-dimensional standing waves, hexagons, and squares. (Hexagons are of course also found for Rayleigh–Bénard convection, but only by departing from the Boussinesq limit of depth-independent physical properties, see for example [2].)

A great deal of flexibility is also afforded by the possibility of modifying the nature of the forcing. For example, in the case where a superposition of two commensurate frequencies is used, quasicrystalline patterns can be produced, i.e. patterns with normally disallowed rotational symmetry [3,4]. An impressive variety of patterns can be obtained by varying the spectral composition of the forcing. Some of this variety is a consequence of modifying the strengths of nonlinear interactions between distinct wave modes or patterns.

At the same time, it must be acknowledged that the surface wave system also has certain disadvantages. Theoretically, the problem is more difficult because of the free surface. Numerical computations are also problematic; the primary pattern is oscillatory so that considerable time resolution is required to study patterns that evolve. Also, lateral boundaries can be influential if the viscosity is low. Raising the viscosity reduces the correlation length and the influence of lateral boundaries, but the requisite acceleration is then high, and the requirement of avoiding deformations of the container therefore leads to massive containers and very large driving forces.

However, it is now possible to do experiments on this system that rival those on Rayleigh–Bénard convection in achieving large aspect ratios, while profiting from the rapid time scale and wave number control. Despite the large number of previous experiments on surface waves, our knowledge of the patterns found near onset as a function of the basic parameters (viscosity, frequency, and driving amplitude) is still somewhat fragmentary *in the large aspect ratio limit.* The purpose of this paper is in part to provide such a systematic survey. We show that a number of novel phenomena become apparent that have not been previously noted. For example, hexagonal patterns occur over a surprisingly wide range of parameters (even for single frequency forcing) and have a different origin than do hexagonal patterns in other pattern forming systems, where quadratic nonlinearities in the amplitude equations are usually responsible.

Our interest goes considerably beyond the question of the patterns obtained near onset. The ability to control the symmetry of the primary pattern provides the opportunity to study secondary instabilities and the onset of spatiotemporal chaos. These phenomena are strongly dependent on the primary pattern symmetry, and also on other variables such as the viscosity. One novel phenomenon discovered recently is a mixed state, in which localized spatiotemporal chaos coexists with ordered stripes [5]. Several other examples will be described below. The overall picture that emerges is quite rich: a number of distinct types of spatiotemporal chaos are realized in this system by modestly varying the driving parameters.

2. Background

The reviews of Cross and Hohenberg [1], and Miles and Henderson [6] provide a good starting point, and we shall only summarize the main points of previous work that are needed for the present discussion of patterns and STC at large aspect ratio. Experimentally, it is known that for low viscosity fluids at high aspect ratio, the dominant pattern near onset is a square pattern formed from two orthogonal standing waves, independent of the shape of the container or the specific fluid. (However, it has been pointed out [3,7,8] that even though the container size is much greater than the

wavelength, the boundaries seriously perturb the patterns if the viscosity is low.) At high viscosities, on the other hand, the patterns are strikingly different, with quasi-1D striped patterns dominating at onset [3,9]. Stripes can also occur in the form of spirals [10].

There have been several different observations of hexagonal (and triangular) patterns [4,11,12]. However, the various published experiments do not provide a clear picture of the ranges of parameters where hexagonal patterns occur, and indeed they are not all mutually consistent with each other. Quasicrystalline patterns have also been noted for single frequency forcing, but again a full discussion of the conditions for obtaining them is lacking [4,12]. (As already pointed out, quasicrystalline pattern can also be created with multi-frequency forcing [3], a situation that we do not treat in this paper.) A comprehensive picture of the preferred patterns for Faraday waves near onset thus remains elusive.

Theoretical discussion of patterns near onset has mainly responded to the experimental observations. The primary approach has been to construct amplitude equations valid near onset for interacting one-dimensional waves, to assume that they are spatially homogeneous and that damping is weak. Using this approach Milner was able to show that the problem is variational. He found that squares are preferred over stripes and hexagons in the capillary wave limit and for low viscosity, in general agreement with experiments. However, this approach has been criticized by Miles [13] and by Zhang [14] as not treating damping properly.

Recently Zhang reconsidered the problem of the patterns near onset at low viscosity and infinite depth [14]. He carefully considers the nature of the viscous damping, and shows that linear viscous terms in the fluid equations can produce nonlinear damping terms in the amplitude equations. The physical origin of this phenomenon is the nonzero irrotational shear stresses at the free surface, which lead to a thin viscous boundary layer and modify the effective boundary condition at the free surface.

Zhang considers a thin fluid layer in the limit of high Reynolds number Re, which is appropriate at the frequencies of interest. Reasoning that nonzero irrotational shear stresses at the free surface lead to a thin viscous boundary layer, he introduces a quasipotential approximation that leads to effective boundary conditions at the free surface. This involves neglecting terms of order $Re^{-3/2}$ in the Navier–Stokes equations. Further simplifications are introduced by neglecting all nonlinear viscous terms. Standing wave amplitude equations are then derived from a double perturbative expansion in the dimensionless driving amplitude and the linear damping parameter. For uniform patterns, these amplitude equations have a gradient form which makes it possible to calculate a Lyapunov functional. By minimization of the Lyapunov functional, the symmetry of the resulting optimal pattern can be determined under given conditions. However, *stability* of the optimal solutions cannot be determined in this way.

The main result of this investigation is to emphasize the important role played by triad resonances involving three wave modes. The condition for obtaining such resonances is strongly frequency-dependent, especially in the regime where capillary and gravity restoring forces are both significant. As a result, Zhang finds that square patterns are destabilized below a certain frequency in favor of hexagonal patterns. He also shows that quasicrystalline patterns have lower values of the Lyapunov functional in certain limited viscosity (or frequency) ranges, but it is unclear that they would be stable. We compare these predictions to experimental observations later in this paper.

Beyond the wave onset region, the transition to spatiotemporal chaos has also been the subject of a number of experimental investigations. Again, the experimental picture is somewhat complex. The primary known mechanism for the transition is a transverse amplitude modulation (TAM) first described by Milner [15]. This instability appears to mediate the transition both for the stripe patterns [9] and the square patterns [16] at least for some viscosities. However, Daudet et al. [9] noted that the modulations produced by the TAM instability are often oscillatory rather than stationary as expected from the theory. These investigators, and previously Bosch et al. [12,17], have emphasized that the nucleation of

defects sometimes plays a significant role in the transition to STC. These variable observations leave one with the overall impression that the transition to STC is not only poorly understood in this system, but is also rather incompletely characterized experimentally. One problem is that the large number of parameters (viscosity, frequency, depth, and container geometry) makes it difficult to compare different experiments. There is apparently no single transition mechanism; rather, it is necessary to elucidate several different ones applicable to different regimes.

Naturally, these different types of transitions to STC lead to quite different observations for the statistical properties well into the chaotic regime. Most of the experimental studies of statistics have been made at low viscosity. For the square pattern, statistical measurements by Tufillaro et al. [16] showed a well-defined transition to disordered waves; the translational correlation length falls dramatically at the transition, and orientational correlations also decline. The probability distribution of individual fluctuating spectral components at wave number k is Gaussian in the chaotic regime. On the other hand, Bosch et al. [12,17] report that the spectral fluctuations can be non-Gaussian at large wave number due to the presence of coherent structure [12]. Finally, we note the observation of Gluckman et al. that disordered fluctuating patterns retain sufficient phase coherence to produce spatially periodic time averages well into the chaotic regime [7,8]. However, it is unknown whether any of the low viscosity observations of this section would persist in a larger system, and they may not be relevant at higher viscosity.

3. Experimental methods

The experiments are conducted in a 32 cm diameter circular container made of Delrin [18]. The container is designed to minimize vibrational excitation, and is hence rather massive, about 11 kg. It is driven vertically with sinusoidal acceleration at a single frequency. The Vibration Test Systems electromagnetic shaker is capable of producing a peak force of about 2200 N; such high forces are needed because of the large mass. Harmonic content is essentially negligible because computer control of the driving signal forces the measured acceleration to match the desired waveform. Accelerations of 15 times the gravitational acceleration ($15g$) can easily be achieved, and the frequency can be varied from 20 Hz to more than 200 Hz. The inhomogeneity in the driving acceleration is less than $\pm 2\%$. (Efforts to reduce it further were not successful.) The dimensionless driving acceleration $\varepsilon = (a - a_c)/a_c$ is monitored via an accelerometer attached to the mounting structure below the cell. The absolute acceleration is also known to be within about 1%.

The fluid consists of silicone oil of various viscosities in a layer 0.3 cm deep. For this depth h the fluid is pinned to the boundary by a sharp corner, and meniscus waves at the driving frequency are minimized. Water at 25.0 ± 0.1°C is circulated through the container to maintain a fixed viscosity.

The patterns formed at the surface of the fluid are imaged using a 512×512 pixel Dalsa variable scan CCD camera controlled by the same computer that produces the driving waveform. The camera allows exposure times as short as 10^{-3} s to be realized if necessary, but an exposure time equal to one fluid period (two driving cycles) is generally used. The phase of the data acquisition is fixed with respect to that of the vertical acceleration. Dark images (obtained with the shutter closed) are subtracted to improve the picture quality. Lighting is provided by a circular ring of 58 lamps at the center of which the camera is located. For sufficiently large wave amplitudes this results in the antinodes being bright and nodes dark. (In fact, the bright regions are not quite antinodes, but rather correspond to a surface slope of 4.2°. However, the lateral displacement of the intensity maxima from the antinodes is less than one pixel, except when the amplitude or frequency is particularly low.)

4. Patterns near onset as a function of viscosity

4.1. Uniform primary patterns

To study the patterns formed above onset, we varied the kinematic viscosity v over the range 0.04–

Table 1
Summary of the pattern symmetries observed just above onset as a function of viscosity and driving frequency

Viscosity ($cm^2 s^{-1}$)	Low ($f_o < 25$ Hz)	Intermediate ($25 < f_o < 50$ Hz)	High ($f_o > 50$ Hz)
0.04	Hexagons	Squares	Squares
0.1	Hexagons	Squares	Squares
0.2	Hexagons	Squares	Squares
0.3	Hexagons	Squares	Stripes
0.5	Hexagons	Squares	Stripes
1.0	Hexagons	Short Stripes	Stripes

The boundaries between different symmetries are approximate. See also Figs. 2–4.

$1.0\,cm^2\,s^{-1}$. The observed patterns depend not only on v but also on the frequency of excitation, which we denote by f_o. A general classification of the observed patterns just above onset as a function of v and f_o is displayed in Table 1. Hexagonal patterns are observed at low f_o over the entire range of v. At high f_o (>50 Hz) square patterns are observed for $v < 0.02\,cm^2\,s^{-1}$, and stripe patterns are observed for higher v.

Examples of the uniform primary patterns observed near onset are shown in Fig. 1. These patterns were obtained by slowly increasing the driving acceleration at a fixed driving frequency and then waiting for a steady state to be reached. The patterns typically require a few minutes to equilibrate after the acceleration is incremented about 1% beyond onset. At the lower viscosities, the patterns tend to be irregular (lacking a single symmetry) very near onset, and are always initiated at the center of the cell. This observation implies that the cell boundary is influential in determining the threshold patterns even in a large layer for *low* viscosity, as expected. Inhomogeneity of the driving acceleration is apparently unimportant at low viscosity.

At high viscosity, on the other hand, the pattern first appears near the boundary and is sensitive to inhomogeneity of the acceleration. It then grows as the acceleration is increased until it covers the entire surface. The range of ε over which the pattern develops is comparable to the measured inhomogeneity. (However it has also been claimed that localized waves may be intrinsic near onset under some conditions [19]. We are unable to resolve the question.)

The stripes are clearly textured (curved) above onset, as shown in Fig. 1(c). This boundary-induced curvature, which is caused by the apparent preference of the stripes to be nearly perpendicular to the boundary, is a *nonlinear* effect, as in Rayleigh-Bénard convection [2]. In most cases this results in two "focus singularities" at the boundaries. We also noted that the curvature of the stripes at the focus singularity grows with v. The square and hexagonal patterns, on the other hand, do not show long range boundary-induced distortion, though the patterns are perturbed and contain defects within a few wavelengths of the boundary. The absence of boundary induced distortion for the square and hexagonal patterns implies a strong angular selection (at 90° or 60°) for the interacting wave modes that make up these patterns, so that minimization of the Lyapunov functional leads only to localized defects near the boundaries rather than producing long range distortions.

4.2. Phase diagrams (parameter space)

Phase diagrams showing the patterns observed as a function of acceleration and frequency are shown in Figs. 2–4, for three representative viscosities. The phase boundaries between patterns of different symmetry are shown along with the curves denoting the primary instability boundary and fully developed STC. To construct these figures, the acceleration was incremented by $0.05g$ or less, and the frequency by 2.5 Hz at low frequencies and 20 Hz at high frequencies. Note that the boundary between hexagons and squares is tilted, so that as ε is increased, a transition from squares to hexagons can occur. There is also a domain of coexistence of squares and hexagons (see Section 4.5). A regime of TAM which mediates the transition to STC is also shown; this phenomenon is discussed in Section 5.2. The "mixed state" in which localized STC coexists with ordered stripes is discussed in Section 5.2. Note that in these phase diagrams we use the term STC to refer *to fully developed* spatiotemporal chaos. In principle one could include states involving slow defect motion in relatively ordered patterns as STC, but such a choice would obscure important distinctions.

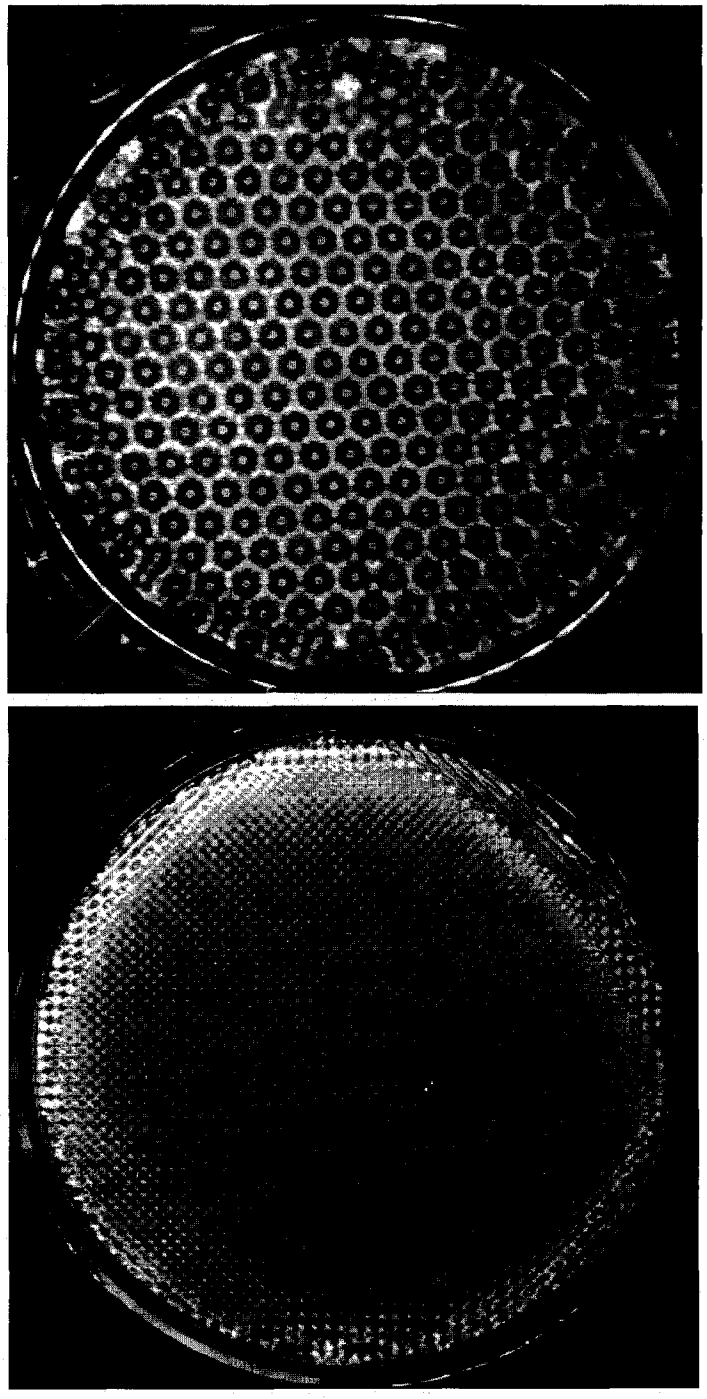

Fig. 1. Examples of the primary patterns formed near onset at large aspect ratio: (a) hexagonal patterns observed at low driving frequencies ($\nu = 0.2\,\mathrm{cm^2\,s^{-1}}$, $f_o = 22.5\,\mathrm{Hz}$); (b) squares ($\nu = 0.1\,\mathrm{cm^2\,s^{-1}}$, $f_o = 35\,\mathrm{Hz}$); or (c) striped patterns ($\nu = 1.0\,\mathrm{cm^2\,s^{-1}}$, $f_o = 45\,\mathrm{Hz}$) found at higher frequencies, depending on the viscosity. The radial intensity variations emanating from the foci in (c) are an artifact due to the discrete nature of the lights.

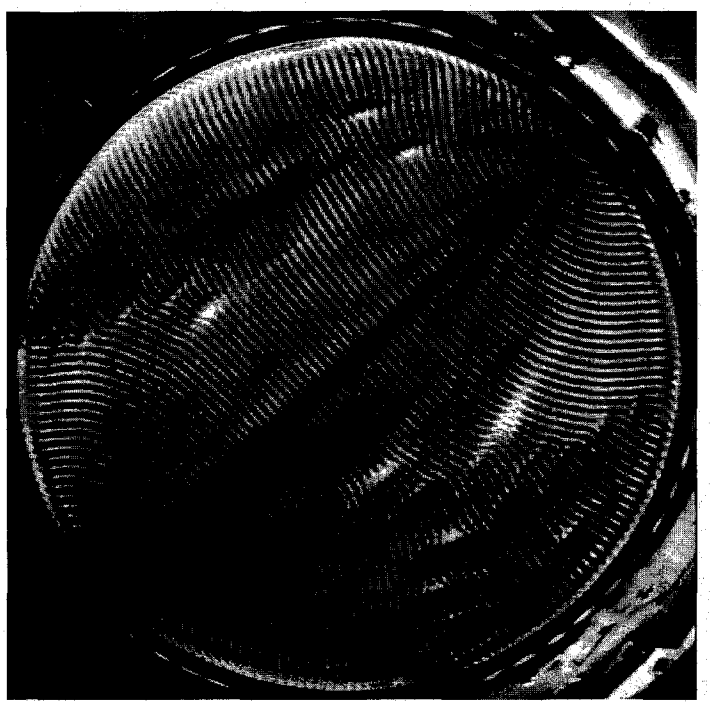

(c)

Fig. 1. (continued)

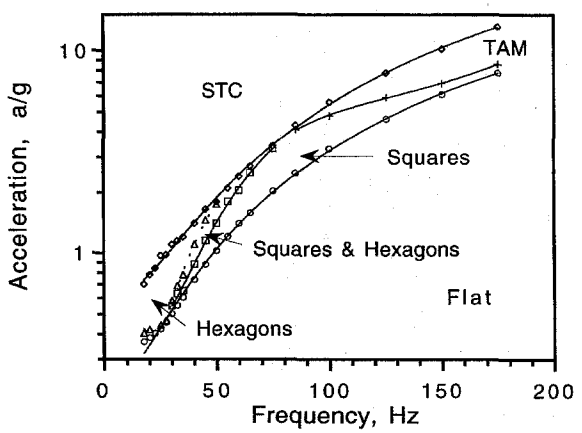

Fig. 2. Parameter space of relatively low viscosity ($v = 0.1\,\mathrm{cm^2\,s^{-1}}$) silicone oil showing observed patterns as a function of driving frequency and amplitude. Similar behavior is observed over the range $0.04 < v < 0.2\,\mathrm{cm^2\,s^{-1}}$. Lines are drawn through the data to guide the eye.

4.3. Short stripes

The striped patterns sometimes appear in a variant that we term "short stripes". This phenomenon, which is shown in Fig. 5, occurs in a regime between the ordinary long stripes and hexagons in the phase diagram of Fig. 4 (where $v = 1.0\,\mathrm{cm^2\,s^{-1}}$). A ring of high amplitude short stripes appears at onset near the boundary of the container; the stripes are always aligned perpendicular to the boundary and their localization is *not* a consequence of inhomogeneity in the driving acceleration. Closer to the center, the waves are of smaller amplitude. (The interior waves appear somewhat brighter in Fig. 6(a) due to a lighting artifact; the finite surface slope required to reflect light into the camera causes the bright areas to move toward the nodes for small wave amplitudes.) Observations of a ring of short stripes were also made by Lioubashevski et al. [19] in a shallow layer of highly viscous fluid. If the driving amplitude is increased, successive rings of short high amplitude stripes are added as shown in Fig. 5(b). The pattern contains many defects which are created and destroyed on a slow time scale (tens of seconds).

The length of the stripes increases with frequency, becoming comparable to the diameter of the container

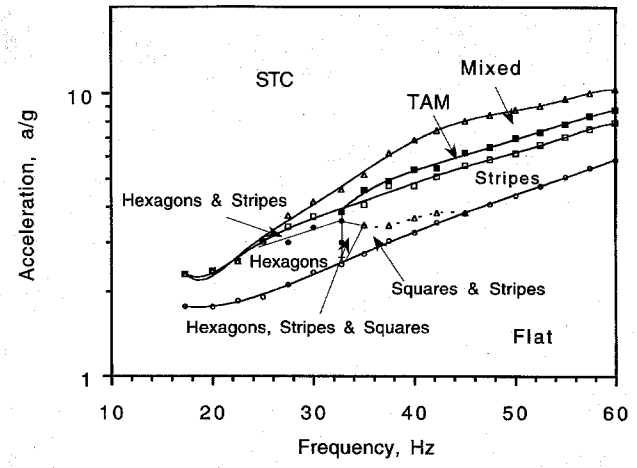

Fig. 3. Parameter space for $\nu = 0.5\,\mathrm{cm^2\,s^{-1}}$. A similar diagram is obtained at $0.3\,\mathrm{cm^2\,s^{-1}}$. Here squares patterns are seen only at intermediate frequencies and low ε. A *mixed* state is observed for which spatiotemporal chaos coexists with laminar stripes.

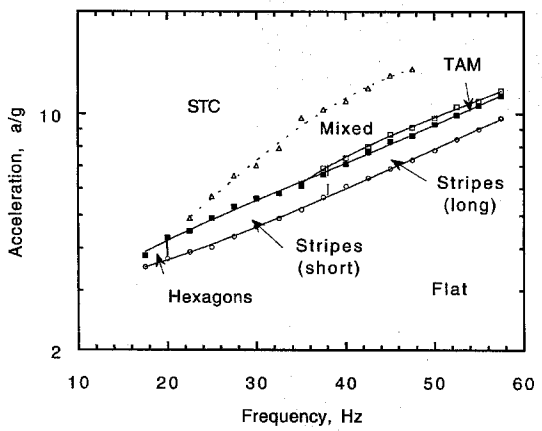

Fig. 4. Parameter space at the highest viscosity, $\nu = 1.0$ $\mathrm{cm^2\,s^{-1}}$.

at about $f_0 = 40\,\mathrm{Hz}$. An intermediate case is shown in Fig. 5(c). The time dependence of the stripes becomes slower as they lengthen, presumably because the defect density is also reduced.

4.4. Phase defects in hexagonal patterns

Defects of various kinds occur in these patterns. One of the more striking is the π phase defects found in hexagonal patterns; these are associated with the subharmonic nature of the waves. The phenomenon is illustrated in Fig. 6, where images averaged over one drive period (or half the wave period) are presented. A hexagonal lattice formed just above onset is shown in Fig. 6(a). Regions of the surface that are concave upward (i.e. depressed) appear brighter than those that are convex (or elevated). The situation reverses in the subsequent half wave period. The regions on the left and right of Fig. 6(a) differ in their temporal phases by π (relative to the forcing). The density of these domains, or of the π phase defects separating them, depends on ε and fo. A situation with *multiple* π phase defects is shown in Fig. 6(b). We return to the dynamical consequences of these defects in Section 5.1, where we consider hexagonal melting.

4.5. Competition between patterns

Given that two and sometimes three distinct symmetries can occur at the same viscosity, it is important to examine the transitions between these different patterns. We find that domains of different symmetries often coexist an intermediate parameter values. The transitions are generally continuous, with the relative amount of one pattern changing continuously with respect to the other.

An example of the competition between *squares and stripes* is presented in Fig. 7. One of the standing waves comprising the square pattern weakens near the boundary as ε is increased, and the patterns become stripe-like in that region. This domain of stripes

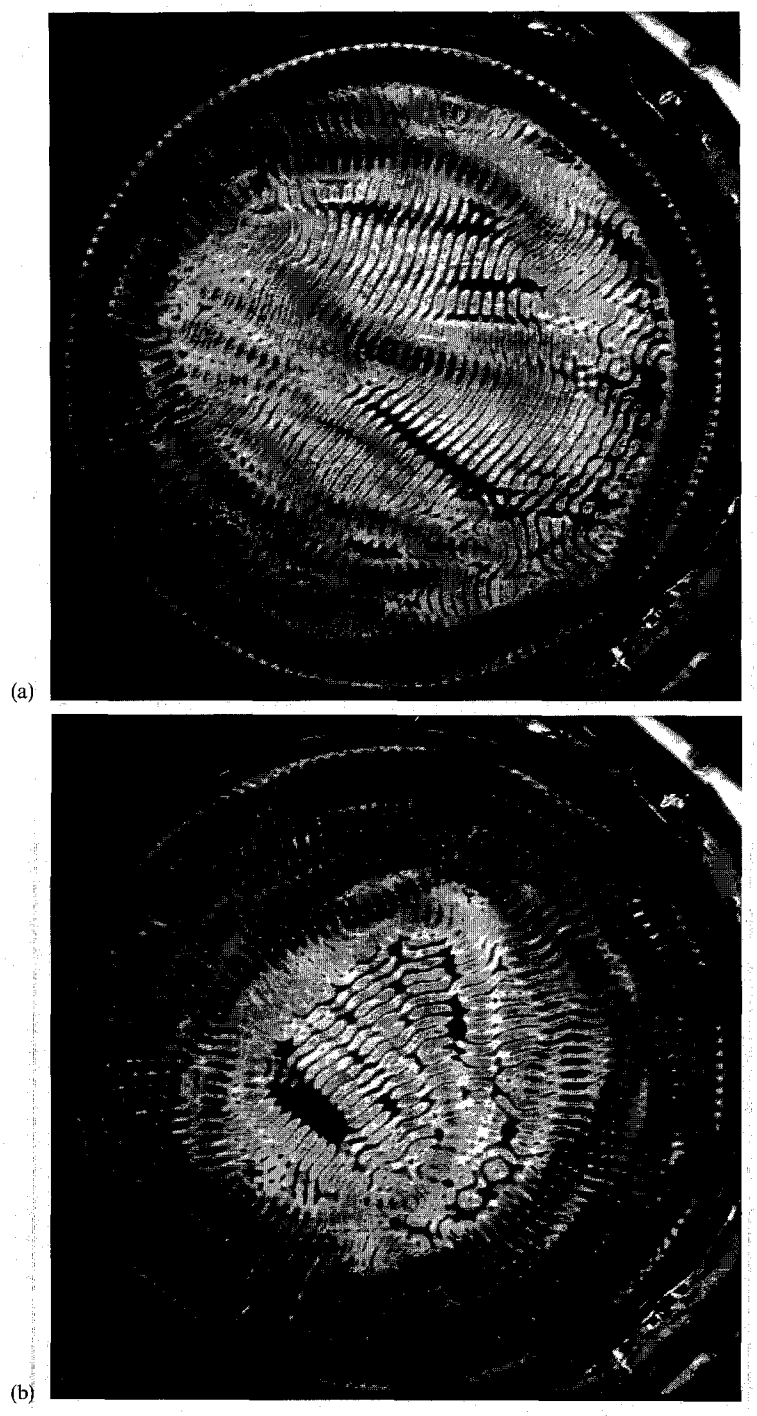

Fig. 5. Short stripes at intermediate driving frequencies for $\nu = 1\,\mathrm{cm}^2\,\mathrm{s}^{-1}$: (a) a ring of high amplitude short stripes formed at the boundary ($f_0 = 30\,\mathrm{Hz}, \varepsilon = 0.01$); (b) successive rings of stripes added as the driving amplitude ε is increased ($\varepsilon = 0.08$); (c) the stripes lengthen as f_0 is increased ($f_0 = 35\,\mathrm{Hz}$, $\varepsilon = 0.14$).

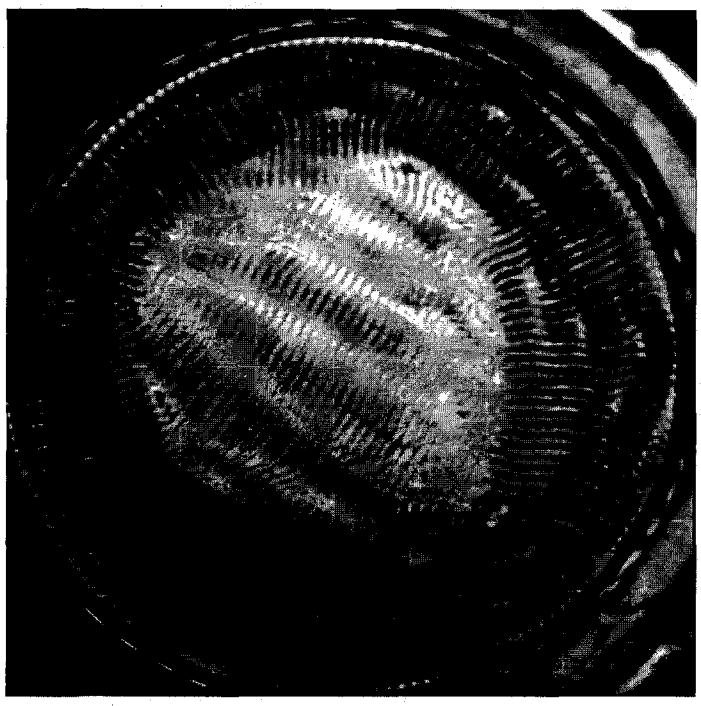

(c)

Fig. 5. (continued)

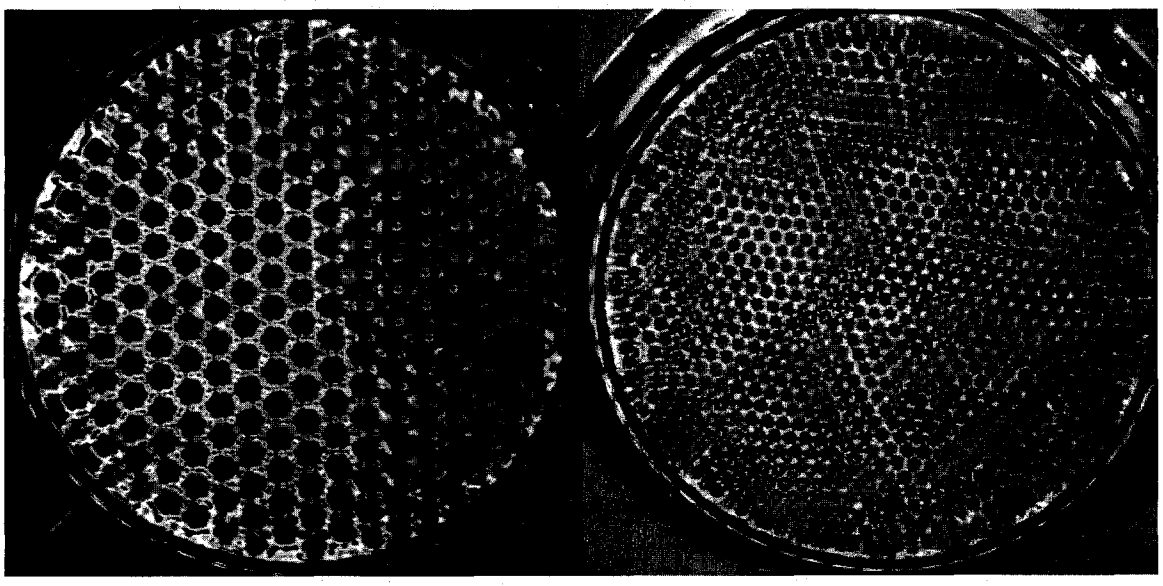

(a) (b)

Fig. 6. Phase defects in hexagonal patterns ($v = 0.2\,\mathrm{cm}^2\,\mathrm{s}^{-1}$): (a) two domains separated by a π phase defect ($f_o = 20\,\mathrm{Hz}$; $\varepsilon = 0.13$); (b) pattern with many phase defects at higher frequency ($f_o = 42.5\,\mathrm{Hz}$; $\varepsilon = 0.34$).

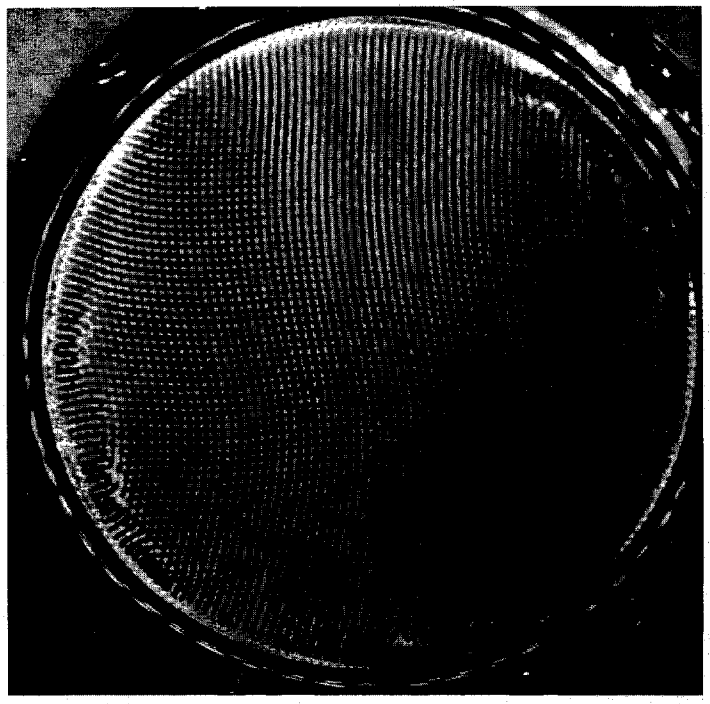

Fig. 7. Coexistence of squares and stripes at the same driving acceleration for $v = 0.5\,\mathrm{cm}^2\,\mathrm{s}^{-1}$ ($f_0 = 42.5$ Hz; $\varepsilon = 0.02$).

expands in area until the entire cell consists of stripes as ε is increased by about 10%. This process corresponds to traversing a vertical line at 42.5 Hz in Fig. 3. The requisite change in ε is much greater than the spatial inhomogeneity in ε, so the coexistence of squares and stripes is an intrinsic effect. We also note that distortions appear in the square patterns of Fig. 7; these are *not* induced by boundaries. The patterns are less rigid than square patterns at low viscosity, and the local orientation wanders, so that the pattern can be locally rhombic.

Coexistence of *squares and hexagons* is also observed; the transition region is shown in Fig. 8. As a function of ε, fracture like defects first appear in an almost perfect square lattice; an increase in ε leads to additional defects and the appearance of hexagons at these locations. Therefore hexagons and squares are seen to coexist, and the hexagonal regions become increasingly prominent as ε is increased.

At moderate viscosities, *all three basic symmetries* coexist over a finite frequency and amplitude range: hexagons, stripes, and squares. An example of such a pattern is shown in Fig. 9 for $v = 0.5\,\mathrm{cm}^2\,\mathrm{s}^{-1}$. Similar patterns are also observed at $v = 0.3\,\mathrm{cm}^2\,\mathrm{s}^{-1}$. In patterns with coexisting symmetries, stripes predominate near the boundary (and are perpendicular to the boundary), whereas squares and hexagons fill the interior. (However, the squares maybe more accurately described as rhombic, and may arise by deleting one standing wave from the hexagons.) The coexistence of disparate patterns implies that they must have similar values of the Lyapunov functional, if one exists approximately.

5. Transitions to spatiotemporal chaos

The nature of the transition to STC depends strongly on the basic symmetry of the pattern. (a) Hexagonal patterns become orientationally disordered by a process that we describe informally as "melting" because of a (possibly superficial) resemblance to crystal

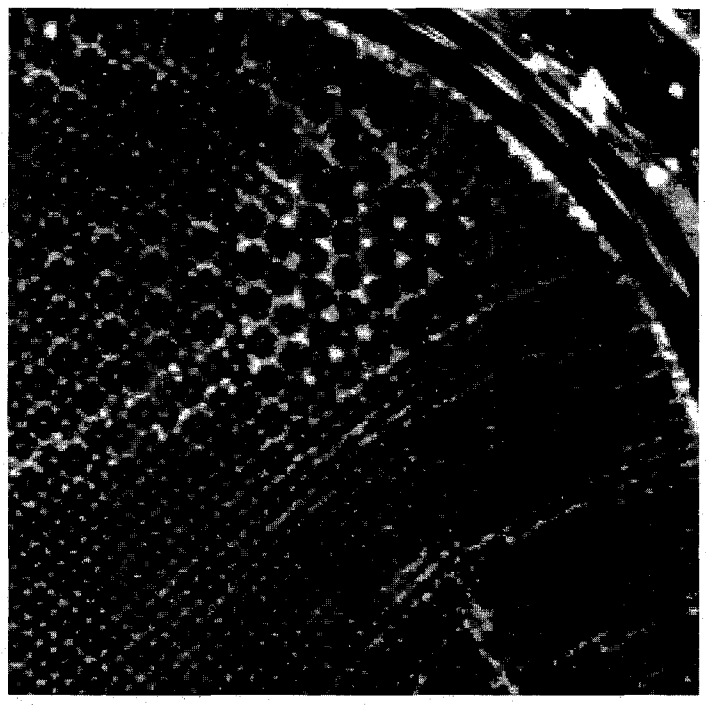

Fig. 8. Coexistence of squares and hexagons. Hexagons from along the fracture lines as ε is increased ($v = 0.2\,\mathrm{cm}^2\,\mathrm{s}^{-1}$, $f_0 = 45$ Hz; $\varepsilon = 0.12$).

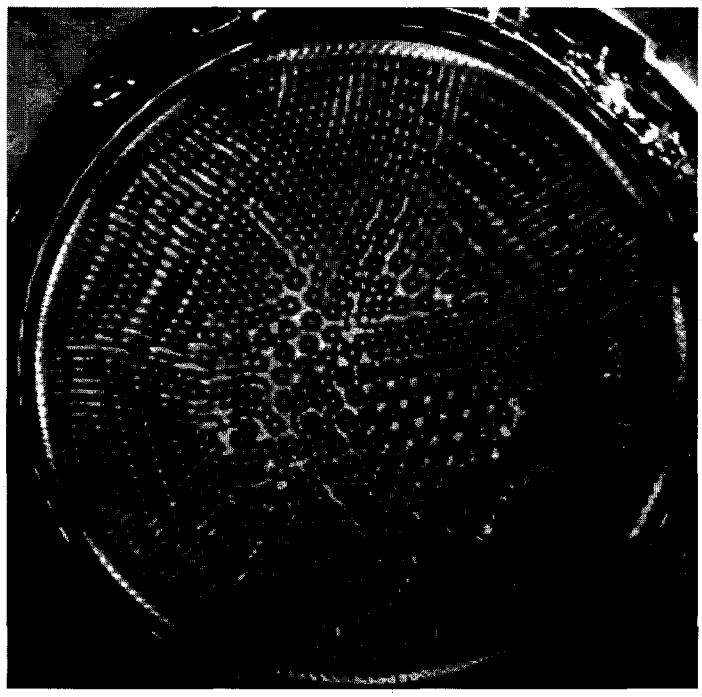

Fig. 9. Weakly time-dependent coexistence of hexagons, squares, and stripes ($v = 0.5\,\mathrm{cm}^2\,\mathrm{s}^{-1}$; $f_0 = 32.5$ Hz; $\varepsilon = 0.26$).

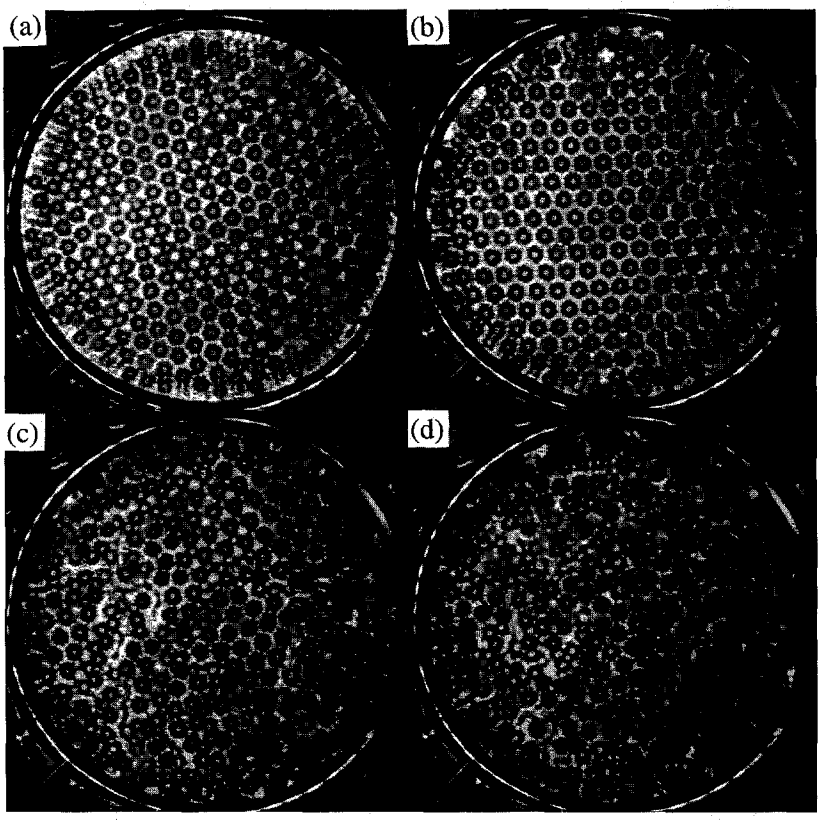

Fig. 10. Hexagonal patterns spanning the "melting" transition as ε is increased ($\upsilon = 0.2\,\mathrm{cm^2\,s^{-1}}$; $f_0 = 22.5\,\mathrm{Hz}$). Images are averaged over two wave periods ($4/f_0$) to reduce noise and the influence of phase defects. (a) $\varepsilon = 0.2$; some phase defects are present. (b) $\varepsilon = 0.4$; the pattern is more nearly perfect than at smaller ε. (c) $\varepsilon = 0.6$; significant orientational disorder is evident. (d) $\varepsilon = 0.8$; spatiotemporal chaos.

melting; π phase defects are involved in this process. (b) Striped patterns display a mixed state in which domains of STC coexist with laminar stripes. The process is initiated by the TAM instability in regions of high curvature. An additional secondary instability, which we call an oscillatory instability, also occurs in this regime. (c) In the regime of coexistence of patterns with distinct symmetries (e.g. squares and hexagons), competition between them leads to nonperiodic time dependence, and a clear onset of STC is difficult to define. We proceed now to a discussion of some of these processes that lead to STC. (The case of the transition to chaos of square patterns was studied in detail by Tufillaro et al. [16] and is not discussed here.)

5.1. Hexagon order/disorder transition

We have noted that hexagonal patterns are observed at low frequency over the entire viscosity range studied. From Figs. 2–4 it is also clear that hexagonal frequency range broadens as υ is reduced. The "melting" or order/disorder transition of the hexagonal patterns was studied by changing ε at fixed f_0 for $\upsilon = 0.2\,\mathrm{cm^2\,s^{-1}}$; sample images spanning this transition are shown in Fig. 10. The hexagonal patterns generally have phase defects for small ε (Fig. 10(a)). These images have been averaged over two wave periods to nearly eliminate the effects of the π phase defects, because they are not the primary source of the orientational disorder that is of interest here.

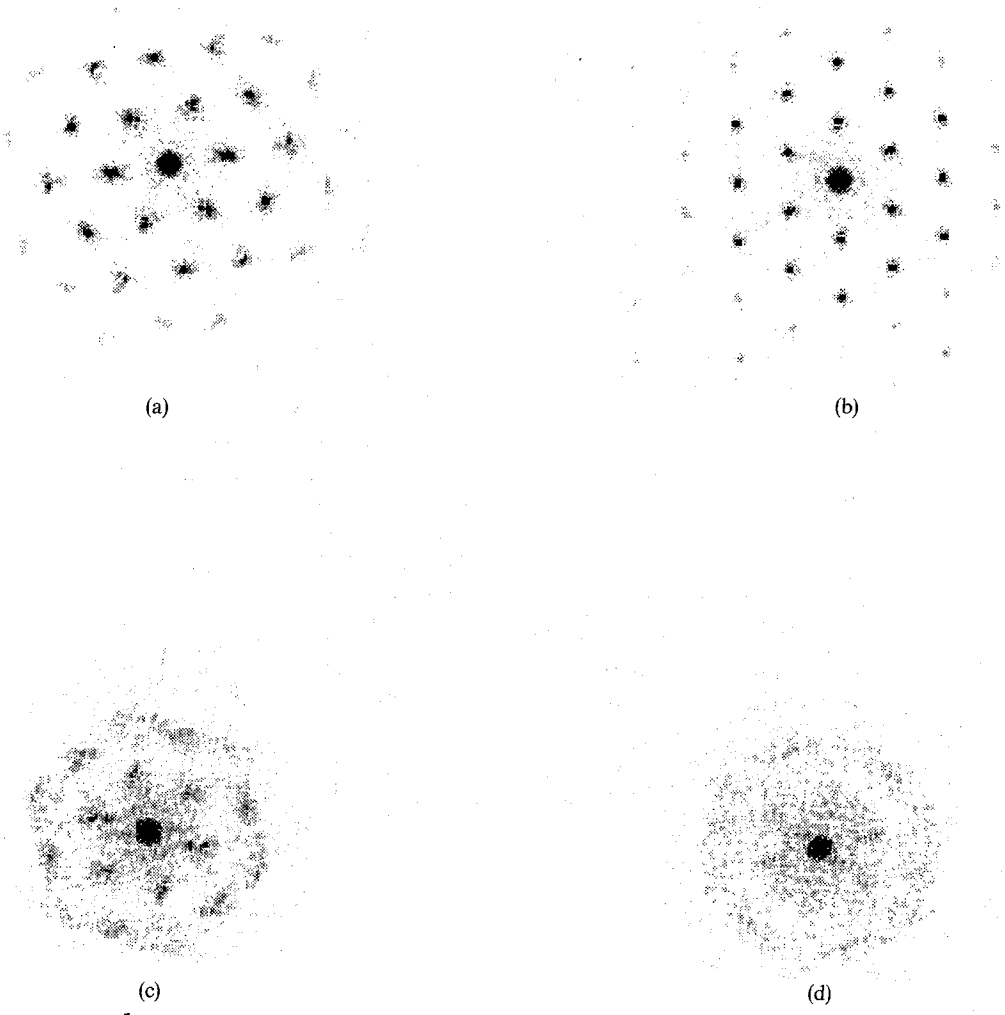

Fig. 11. Power spectra $S(\boldsymbol{k})$ of the images shown in Fig. 10 (for $\varepsilon = 0.2$, 0.4, 0.6, and (0.8) increasingly isotropic as ε is increased beyond 0.4.

Though time-averaging makes the domains indistinguishable, the boundaries between them are evident in Fig. 10(a).

The hexagons form an almost perfect lattice at finite ε (e.g. 0.4 as in Fig. 10(b)). A further increase in ε leads to orientational disorder, as shown in Fig. 10(c), though domains of nearly perfect hexagonal order are still evident. In Fig. 10(c), for which $\varepsilon = 0.8$, extended ordered domains are essentially absent and the transition is nearly complete.

Fourier analysis is used to explore the nature of the order/disorder transition. Power spectra $S(\boldsymbol{k})$ of the images of Fig. 10 are presented in Fig. 11. The increased long range order at $\varepsilon = 0.4$ compared to *lower* values (Fig. 11(b)) is manifested by a sharpening of the six spots corresponding to the three standing waves that compose the hexagonal lattice. However *a further* increase in ε to 0.6 (Fig. 11(c)) leads both to broadened spots and to more spectral power near the origin in $\boldsymbol{k}$-space.

We characterize this transition process quantitatively in several ways. First, the mean wave number $\langle k \rangle$, is computed:

$$\langle k \rangle = \frac{\int k S(\boldsymbol{k})\, \mathrm{d}^2 k}{\int S(\boldsymbol{k})\, \mathrm{d}^2 k}. \tag{1}$$

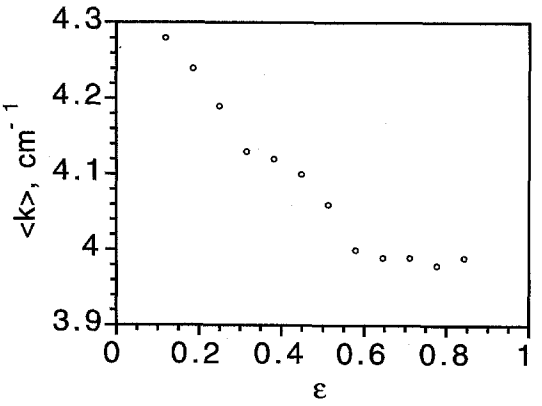

Fig. 12. The mean wave number decreases as ε is increased through the melting transition.

The integral is actually computed only over an annulus in k space that includes the six main hexagonal spots. (The width of the annulus is about $0.5k_o$, where k_o is the magnitude of the wave number of the spots *at onset*.) The mean wave number decreases slowly with ϵ as shown in Fig. 12). Such a shift in the mean wave number is not uncommon, and has been seen for example in spiral defect chaos in thermal convection [20].

To characterize the melting (and loss of anisotropy) of the hexagonal pattern, we compute the angular spectral distribution $P(\theta)$ by integrating $S(\boldsymbol{k})$ over the radial segment from $0.75k_o$ to $1.25k_o$:

$$P(\theta) = \int S(\boldsymbol{k})\, \mathrm{d}k. \tag{2}$$

This function is shown in Fig. 13 for three values of ε spanning the melting transition. The strong peaks are attenuated with increasing ε. This process can be studied quantitatively by computing the *angular anisotropy* A, which we define as follows:

$$A = \frac{\sqrt{\langle P^2(\theta)\rangle - \langle P(\theta)\rangle^2}}{\langle P(\theta)\rangle}. \tag{3}$$

To measure A, we stepped the acceleration by intervals of 0.05 g at each f_o, waited 10 min, and then acquired 10 images averaged over four drive periods at 1 min intervals. Subsequently, $S(\boldsymbol{k})$, $P(\theta)$, and A were computed for each image, and the average of A over the 10 images was utilized. The variation of A with ε is shown in Fig. 14 for runs made at three different driving frequencies. The transition to the isotropic state is *continuous* but reasonably well defined, and is centered at the same ε for each of the three frequencies. The finite value of A obtained at large ε is probably due to measurement noise.

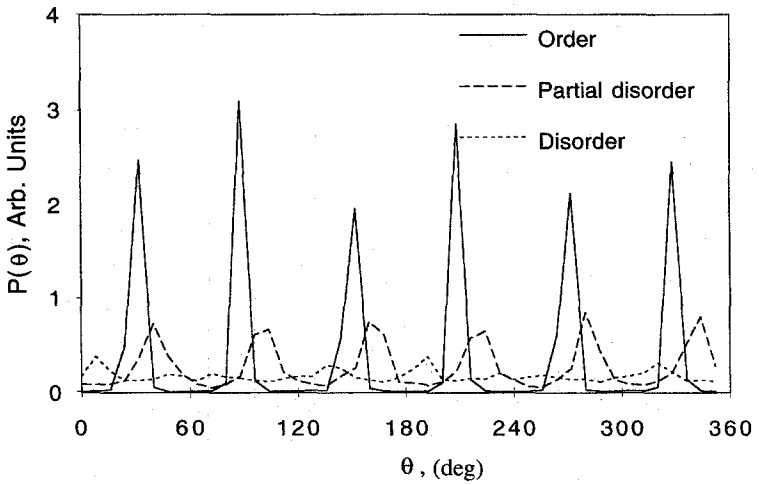

Fig. 13. Angular dependence $P(\theta)$ of the spectral structure function over a band centered at the mean wave number k_o. Six peaks are observed which decrease in amplitude as ε is increased through the melting transition.

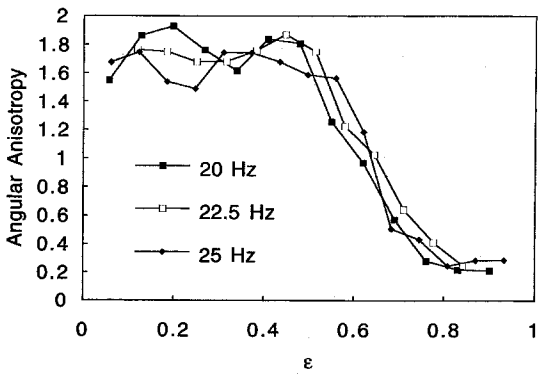

Fig. 14. Angular anisotropy A defined in Eq. (3). This quantity reveals a continuous but well-defined melting transition that is approximately independent of driving frequency over the range shown.

5.2. *Localized spatiotemporal chaos of striped patterns: the mixed state*

The development of STC of the striped pattern is strikingly nonuniform in space; it involves a mixed state in which localized STC coexists with ordered stripes. TAMs play an important part in the development of this state. This secondary instability was first discussed theoretically by Milner and was observed in several previous investigations [15,16]. However, the large aspect ratio of the present experiments leads to different results. The parameter range over which TAMs are observed is shown in Figs. 3 and 4 for the striped pattern. The modulations are first observed near the focus singularities i.e. in the regions of high curvature. At high viscosity the modulations remain confined to the high curvature regions as STC develops with increasing ε. However somewhat lower viscosity, the modulations propagate all the way across the cell, as shown in Fig. 15. The modulation amplitude increases with ε and defects are created which climb and glide towards the focus singularities. The defect density increases with ϵ leads to *STC near the focus singularities*. This scenario of the development of STC via the TAM instability is different than that observed by Daudet et al. [9], probably because their smaller aspect ratio did not allow curvature to develop.

The resulting mixed state is shown in Fig. 16. The dark regions near the boundary have high wave

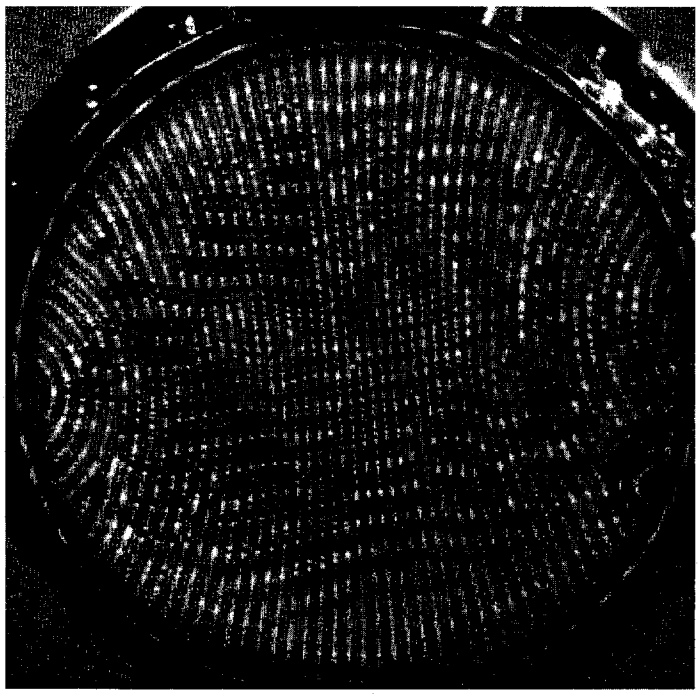

Fig. 15. Transverse amplitude modulations in the striped pattern ($\upsilon = 0.5\,\mathrm{cm^2\,s^{-1}}$; $f_0 = 55\,\mathrm{Hz}$; $\varepsilon = 0.48$).

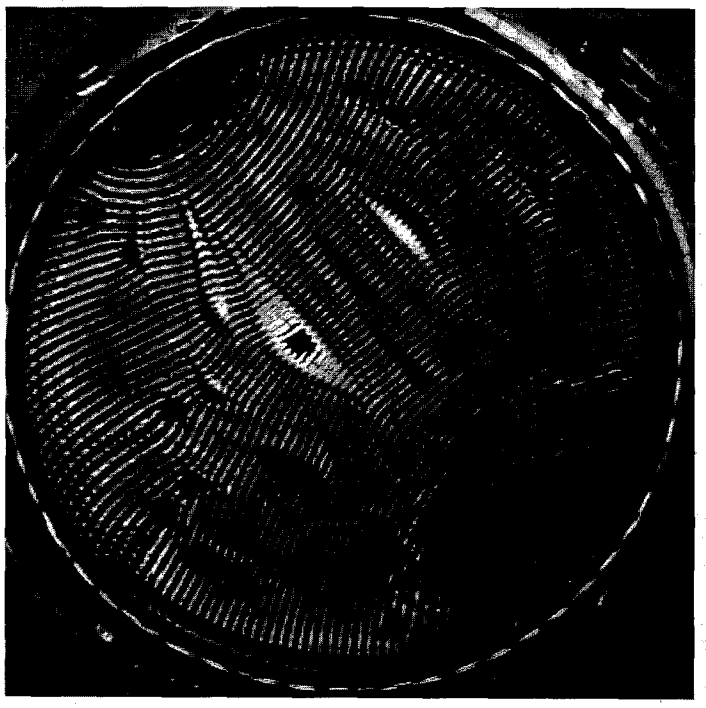

Fig. 16. Coexistence of localized spatiotemporal chaos with ordered stripes ($v = 1.0\,\mathrm{cm}^2\,\mathrm{s}^{-1}$; $f_o = 45\,\mathrm{Hz}$; $\varepsilon = 0.36$). The STC domains are darker because they scatter more light away from the camera.

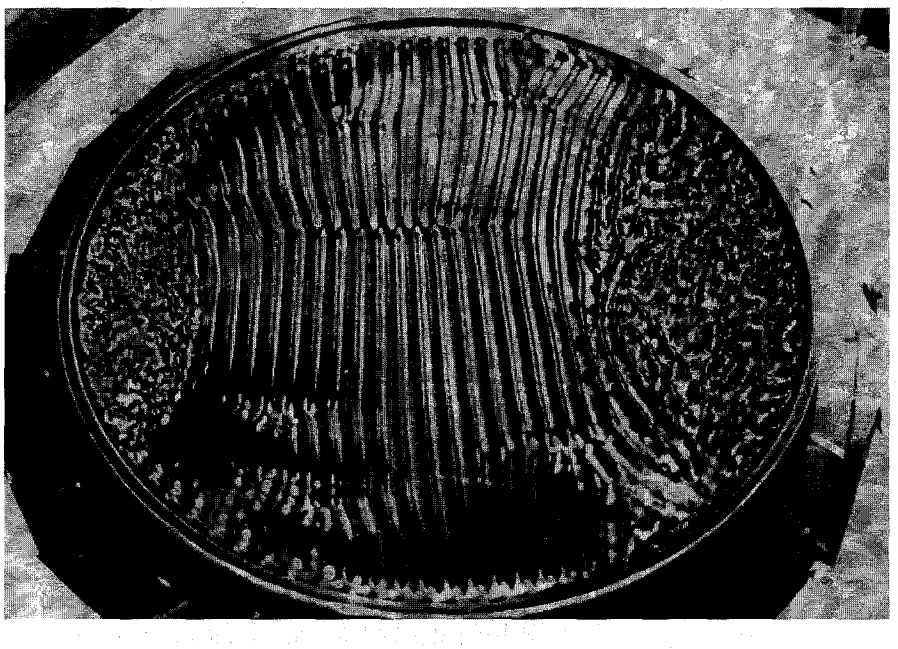

Fig. 17. Inclined view of the mixed state; the wave amplitudes are much larger in the STC domains ($v = 1.0\,\mathrm{cm}^2\,\mathrm{s}^{-1}$; $f_o = 45\,\mathrm{Hz}$; $\varepsilon = 0.45$).

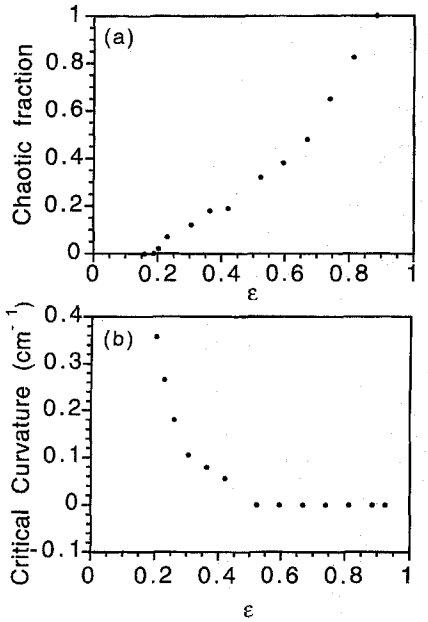

Fig. 18. (a) Chaotic fraction of the mixed state as a function of ε. The entire cell is eventually chaotic. (b) Curvature at the boundary of the chaotic domains as a function of ε ($\upsilon = 1.0\,\mathrm{cm^2\,s^{-1}}$; $f_0 = 45\,\mathrm{Hz}$).

amplitudes and short space and time scales; on the other hand, the striped portion of the pattern is only slowly time-dependent due to the presence of a few defects. An inclined view of the mixed state is shown in Fig. 17. The amplitudes in the domains of STC are much higher than in the striped domains. Droplets are also seen to be ejected occasionally in this region.

In a detailed study [5] of the mixed state, we found that proportion of the pattern covered by the STC domains increases smoothly until the entire cell is chaotic (see Fig. 18(a)). The chaotic fraction is independent of the manner in which the mixed state is induced (quasistatic changes versus sudden steps in ε). In the case of step changes from negative to positive ε, a circular domain of STC forms initially at the center of the cell and later breaks up and migrates to the boundaries.

The chaotic domains always develop in the high curvature regions. (This effect is most evident at high viscosity.) This leads us to introduce the concept of an ε-dependent "critical curvature" which seems to be necessary to produce these domains. This quantity is shown in Fig. 18(b); it decreases with increasing ε.

It must be also noted that although the curvature of the stripes appears to be induced by the circular boundary, it is not specific to this geometry. For example in a square container the focus singularities are expected to form at the vertices and hence a mixed state is still expected.

5.3. *Secondary oscillatory instability of striped patterns*

The striped pattern in the mixed state shows an additional secondary instability that seems not to have been noted before: an oscillatory instability that deforms the striped wavefronts. This phenomenon is observed in a limited viscosity range υ=0.3–0.5 $\mathrm{cm^2\,s^{-1}}$ and below a certain frequency (50 Hz for 0.5 $\mathrm{cm^2\,s^{-1}}$). An example is shown in Fig. 19. The waves visible on the stripes are mostly standing waves, but they also travel slowly toward the outer cell boundary. These oscillations are seen only in the mixed state, and appear intermittently near their threshold. The oscillation amplitude increases with ε. The wavelength of the oscillations is found to fluctuate by about 20% even within the same pattern, and no clear trend with ε was seen over the limited range in which the phenomenon occurs. This instability superficially resembles the oscillatory instability of Rayleigh–Bénard convection rolls [21].

6. Discussion and comparison to theoretical work

In this section we discuss the data in terms of relevant theoretical models. However, available models are not capable of explaining many of the phenomena we observe.

6.1. *Onset patterns*

Let us first consider the symmetries of the various onset patterns we have noted (Fig. 1 and the phase diagrams of Figs. 2–4). They are similar to those formed in thermal convection at large aspect ratio. However, we find hexagons near onset over a rather

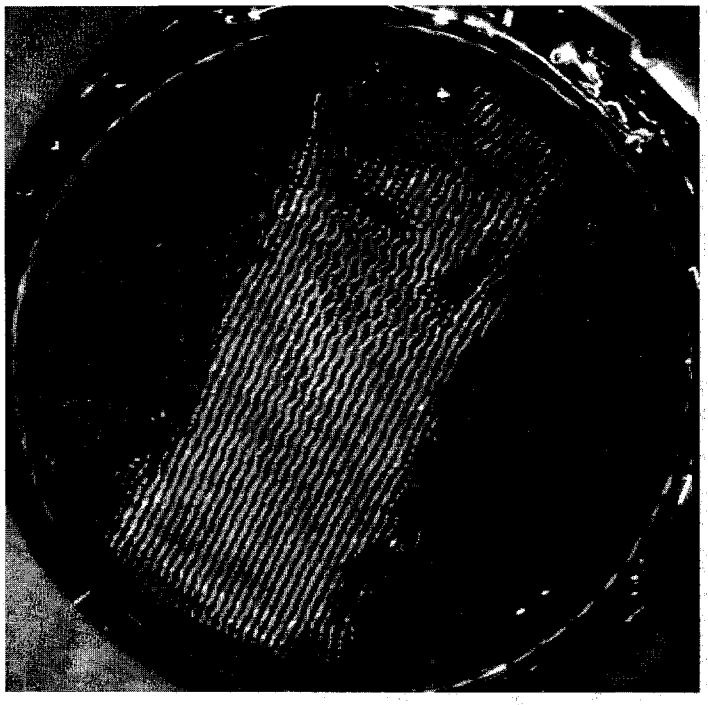

Fig. 19. Example of the secondary oscillatory instability that deforms the stripes within the mixed state at intermediate viscosities ($v = 0.5\,\mathrm{cm^2\,s^{-1}}$; $f_0 = 45\,\mathrm{Hz}$). The waves on the stripes are mostly standing but travel slowly.

broad range of parameters. At first glance, this is surprising in the context of the general theory of pattern formation. In most cases, e.g. in thermal convection [22], hexagons are explained by quadratic nonlinear terms in the amplitude equations. However such terms are *excluded* for single frequency forcing of Faraday waves by the subharmonic symmetry [3]. At the level of amplitude equations, the origin of the hexagons in the experiments described here must be at higher order. (For multi-frequency forcing, on the other hand, quadratic terms are introduced and hexagons appear by the usual mechanism [3].)

Zhang [14] has proposed (for small damping and neglecting finite depth effects) that an explanation for hexagons can be found in terms of the relative balance between gravitational and capillary forces at different frequencies, which affects the triad resonances between wave modes, as explained in Section 2. Consider the dispersion relation

$$\omega^2 = \tanh(kh)\,(gk + Tk^3/\rho), \tag{4}$$

where ω is the wave frequency (half the excitation frequency f_0), g is the acceleration due to gravity, T is the surface tension, and ρ the density. In this equation, the gravitational term is larger than the capillary term for $f_0 = \omega/\pi < 27\,\mathrm{Hz}$ (for silicone oil). The relative importance of gravitation can be changed by tuning the driving frequency.

Zhang [14] predicts that a strong triad resonance occurs near $f_0 = 27\,\mathrm{Hz}$ and that it *disfavors* square patterns at those frequencies, so that hexagonal patterns or other higher symmetry patterns are more stable (depending on the viscosity). This is generally consistent with our experiments. However the range of viscosity over which hexagons are observed is *greater* than expected, as may be seen from the first two columns of Table 2. In the theory the triad resonances are more strongly damped at higher viscosities so that hexagons are not expected at onset above $v = 0.15\,\mathrm{cm^2 s^{-1}}$. On the other hand, the effects of finite depth would have

Table 2
Comparison of experimental observations for onset patterns with the theoretical predictions of Zhang (which are not applicable at high viscosity)

Viscosity ($cm^2 s^{-1}$)	Theory ($f_o = 27$ Hz)	Experiment ($f_o = 27$ Hz)	Theory ($f_o \gg 27$ Hz)	Experiment ($f_o = 50$ Hz)
0.04	Eight-fold quasipattern	Hexagons	Squares	Squares
0.1	Hexagons	Hexagons	Squares	Squares
0.2	Squares	Hexagons and squares	Squares	Squares
0.5	(Not applicable)	Hexagons	(Not applicable)	Stripes
1.0	(Not applicable)	Short Stripes	(Not applicable)	Stripes

to be included in the calculations before a more quantitative comparison could be made to the experiments regarding the domains of occurrence of hexagons and squares. We also note that the theory is valid only at low viscosity and is hence not relevant to the occurrence of stripes at high viscosity. In fact, no explanation has been advanced for the striped patterns. (Predictions of stripes being preferred to squares *at low* viscosity [23] are inconsistent with experiments.)

One important caveat to the comparison with Zhang's predictions is the fact that the approximation of irrotational flow fails when the viscous layer of thickness h_v becomes comparable to the fluid depth h:

$$h_v = \sqrt{2v/\omega}. \tag{5}$$

This issue has also been discussed briefly by Kumar [24]. The viscous depth as a function of viscosity at two driving frequencies is presented in Fig. 20. For $h = 0.3$ cm and small v the viscous depth is at least 10 times smaller than h, but at high v and low frequencies, h_v is significant. Since the viscous depth decreases with decreasing viscosity, and since hexagons are present over a *larger* frequency range at lower viscosity, it seems clear that finite depth does not cause the hexagons to appear.

As a further check for depth effects, we conducted a set of experiments in a deeper layer with $h = 0.9$ cm for $v = 0.2\,cm^2 s^{-1}$. We find that the minimum frequency for squares (about 27 Hz) is not much changed. On the other hand, it is not possible to extend the comparison to very low frequencies because the limited container size (even though large) becomes more important for the deeper layer, and cavity modes predominate over hexagons near onset in that case.

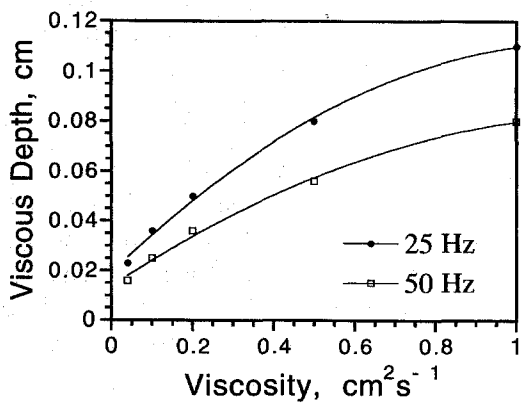

Fig. 20. Viscous layer depth h_v as a function of viscosity v at $f_o = 25$ Hz and $f_o = 50$ Hz. The depth of the fluid used in the experiments is 0.3 cm.

6.2. Nonlinear effects and spatiotemporal chaos

The phase diagrams (Figs. 2–4) obtained in this large aspect ratio system are quite rich. Several novel phenomena have been elucidated, including short stripes (Fig. 5), hexagons with phase defects (Fig. 6), and the coexistence of different symmetries (Figs. 7–9). In general, the transitions between patterns of different symmetry are continuous. The reduction in the importance of boundaries at high aspect ratio leads to a complicated picture of pattern formation in which may factors have to be considered.

A number of distinct transitions to STC occur in this system for different parameter ranges. We have studied two of them in depth: Melting of the hexagonal patterns (Figs. 10–14), and the transition to STC of the striped patterns via the TAM instability (Fig. 15) and the mixed state (Figs. 16–18).

The hexagonal order/disorder transition bears some resemblance to other nonequilibrium transitions to

STC [25], including the transition to STC of the square pattern which was studied by Tufillaro et al. [16]. However, the hexagonal case considered here is the first example in Faraday waves where the container geometry is clearly *not* important. The transition is a continuous one as in some other transitions to STC [20]. Several different physical processes are involved. For example, the π phase defects contribute to the transition, but do not produce orientational disorder. We also noted that "microcrystallites" of local order can be found in the transition region. We propose that the hexagonal melting transition involves a breakdown of the coupling of the standing wave modes to each other. We hope that it might be possible in the future to explore this hypothesis theoretically.

The transition to STC of the striped patterns is also intriguing and leads to an important physical question: why does curvature reduce the stability of the stripes? It should be possible to address this question using suitable model equations. Zhang and Viñals [26] have simulated 2D model equations containing the simplest nonlinearities that produce a stripe-to-STC transition. The equations are solved using periodic boundary conditions and hence uniform straight stripes are obtained below the transition. It might be possible to modify these model equations to take into account the observed curvature dependence of the TAM onset in order to explain the mixed state. The origin of the observed *oscillatory instability* that deforms the stripes (Fig. 19) also merits theoretical attention.

We conclude by noting that the phenomena presented in this paper are all obtained using *single frequency* forcing. With multi-frequency forcing, a considerable variety of additional phenomena occur. Even leaving aside the issue of quasicrystalline patterns, the hexagonal lattices can acquire additional "super-lattice" periodicities and can become anisotropic. These phenomena remain to be explored in depth.

Acknowledgements

We appreciate helpful discussions with W. Zhang. This work was supported by NSF Grant DMR-9319973. W.S. Edwards designed the apparatus and control systems used for this investigation, and B. Boyes provided technical support.

References

[1] M.C. Cross and P.C. Hohenberg, Pattern formation outside of equilibrium, Rev. Mod. Phys. 65 (1993) 851.
[2] E. Bodenschatz, J. de Bruyn, G. Ahlers and D.S. Cannell, Phys. Rev. Lett. 67 (1991) 3078.
[3] W.S. Edwards and S. Fauve, Patterns and quasipatterns in the Faraday experiment, J. Fluid Mech. 278 (1994) 123.
[4] B. Christiansen, P. Alstrom and M.T. Levinsen, Ordered capillary-wave states: Quasicrystals, hexagons, and radial waves, Phys. Rev. Lett. 68 (1992) 2157.
[5] A. Kudrolli and J.P. Gollub, Localized spatiotemporal chaos in surface waves, to be published.
[6] J. Miles and D. Henderson, Parametrically forced surface waves, Ann. Rev. Fluid Mech. 22 (1990) 143.
[7] B.J. Gluckman, P. Marcq, J. Bridger and J.P. Gollub, Time-averaging of chaotic spatiotemporal wave patterns, Phys. Rev. Lett. 71 (1993) 2034.
[8] B.J. Gluckman, C.B. Arnold and J.P. Gollub, Statistical studies of chaotic wave patterns, Phys. Rev. E 51 (1995) 1128.
[9] L. Daudet, V. Ego, S. Manneville and J. Bechhoefer, Secondary instabilities of surface waves on viscous fluids in the Faraday instability, Europhys. Lett. 32 (1995) 313.
[10] S.N. Kiyashko, L.N. Korzinov, M.I. Rabinovich and L.S. Tsimring, Rotating spirals in the Faraday experiment, to be published.
[11] K. Kumar and K.M.S. Bajaj, Competing patterns in the Faraday experiment, Phys. Rev. E 52 (1995) R4606.
[12] E.G.T. Bosch, An experimental investigation of Faraday waves and spatio-temporal chaos, Ph.D. Thesis, Technische Universiteit Eindhoven (1995).
[13] J.J. Miles, On Faraday waves, J. Fluid Mech. 248 (1993) 671.
[14] W. Zhang, Pattern formation in weakly damped parametric surface waves, Ph.D. Thesis, Florida State University (1994).
[15] S.T. Milner, Square patterns and secondary instabilities in driven capillary waves, J. Fluid Mech. 225 (1991) 81.
[16] N.B. Tufillaro, R. Ramshankar and J.P. Gollub, Order–disorder transition in capillary ripples, Phys. Rev. Lett. 62 (1989) 422.
[17] E. Bosch and W. van de Water, Spatiotemporal intermittency in the Faraday experiment, Phys. Rev. Lett. 70 (1993) 3420.
[18] T. Besson, W.S. Edwards and L.S. Tuckerman, Two frequency parametric excitation of surface waves, Phys. Rev. E 54 (1996) 507.
[19] O. Lioubashevski, H. Arbell and J. Fineberg, Dissipative solitary states in driven surface waves, Phys. Rev. Lett. 76 (1996) 3959.

[20] S.W. Morris, E. Bodenschatz, D.S. Cannell and G. Ahlers, Spiral defect chaos in large aspect ratio Rayleigh–Bénard convection, Phys. Rev. Lett. 71 (1993) 2026.
[21] V. Croquette and H. Williams, Nonlinear waves of the oscillatory instability on finite convective rolls, Physica D 37 (1989) 300.
[22] F.H. Busse, The stability of two-dimensional convection and its relation to extremum principle, J. Fluid Mech. 30 (1967) 625.
[23] J. Miles, Faraday waves: Rolls vs squares, J. Fluid Mech. 269 (1994) 353.
[24] K. Kumar, Linear theory of Faraday instability in viscous liquids, to be published.
[25] Q. Ouyang and H.L. Swinney, Transition to chemical turbulence, Chaos 1 (1991) 411.
[26] W. Zhang and J. Viñals, Secondary instabilities and spatiotemporal chaos in parametric surface waves, Phys. Rev. Lett. 74 (1995) 690.